

Supporting Information

Stretching c-axis of Mn₃O₄ Lattice with broadened ion transfer channel for Enhanced Na-Ion Storage

Shiyu Wang^a, Rui Zhao^a, Shuyun Yao^a, Bingcan Li^b, Ruochen Liu^a, Xia Liu^a, Zhenzhen Fu^a,
Dewei Wang^a, ZhiYu Yang^{a, *}, Yi-Ming Yan^{a, *}

Methods

1. Chemicals and reagents

Chemicals and Reagents: Mn(NO₃)₂ were obtained from Shanghai Macklin Biochemical Co., Ltd. Sublimed sulfur were purchased from Aladdin Industrial Corporation. H₂O₂ and NaOH were purchased from Beijing Chemical Works. All reagents were used as received without further purification.

2. Fabrication of MnO₂

Synthesize of precursor MnO₂: 2.863 g Mn(NO₃)₂ was dissolved into 40 mL distilled water, and the pH was adjusted to 9 with 1 mol/L NaOH solution. Then, 4 mL 30% hydrogen peroxide (H₂O₂) was added to the above solution. Subsequently, the solution was ultrasonically treated for 1 h with output intensity of 150 W (low frequency of 40 KHz). The resulted product was filtered and washed with ultrapure water and absolute ethanol. Finally, the as-prepared precipitate was gathered and then dried at 60°C for 6 h. The sample obtained was defined as MnO₂.

3. Fabrication of Ov-Mn₃O₄

Fabrication of Ov-Mn₃O₄: MnO₂ and element sulphur were mixed with the mass ratio of 1:1, and then annealed at 200 °C with the heating rate of 5 °C / min for 2 h in N₂ atmosphere. The resulted product was ultrasonically washed by cyclohexane for three times, and then washed with deionized water. Finally, the sample was dried at 60 °C for 6 h and defined as Ov-Mn₃O₄.



Fabrication of Mn_3O_4 : Mn_3O_4 was prepared with the same process except without the addition of element sulphur.

4. Characterization of the samples

Microstructure were studied using scanning electron microscopy (SEM, FEI Quanta 200) at 20 kV, transmission electron microscopy (TEM; FEI Tecnai G2 20) and HRTEM (JEOL, JEM-2100, 200 kV). X-ray powder diffraction (XRD) patterns were obtained on a Bruker D8 Advance diffractometer with Cu Ka ($\lambda = 0.15406$ nm) radiation and scanning angles (2θ) ranging from 10° to 90° . STEM studies were conducted using a JEOL ARM200F atomic resolution analytical electron microscope equipped with a cold field-emission gun, a new ASCOR fifth order aberration corrector, and Gatan Quantum ER spectrometer. STEM was operated at 200 kV. X-ray powder diffraction (XRD) patterns were obtained on a Bruker D8 Advance diffractometer with Cu Ka ($\lambda = 0.15406$ nm) radiation and scanning angles (2θ) ranging from 10° to 90° . BET surface area measurements were performed through nitrogen sorption on a Quantachrome Instruments NOVA 2,000 high-speed surface area BET analyzer at a temperature of 77 K. Raman spectroscopy was performed on a 532 nm Finder Vista Laser micro-Raman Spectroscopy (Zolix, China). The Fourier transform infrared spectrometer (VERTEX 70) was used to observe the structure of the samples. The surface chemical composition was analyzed using an X-ray photoelectron spectrometer (XPS, PHI Quantera II). JEOLJESFA200 EPR spectrometer was used to obtain the electron paramagnetic resonance (EPR) spectra, and operating parameters were 140 K, 9064 MHz, 0.998 mW, X-band. The Raman spectrum was recorded on a HORIBA Raman microscope with a laser wavelength of 532 nm (LabRAM Aramis, HORIBA Jobin Yvon S.A.S, France) for surface characterization. The electrochemical operando Cell (EC-RAIR-H) is supplied by Beijing Science Star technology Co. Ltd.

5. Electrochemical measurements

Working electrode was prepared by traditional slurry-coating method. 80 wt % active material, 10 wt % carbon black and 10 wt % PTFE was mixed and coated onto carbon cloth with an area of 1 cm². The electrode was then heated at 60 °C for 2 h to evaporate the solvent. Electrochemical measurements were conducted in a general three-electrode configuration in 1 M Na₂SO₄ aqueous electrolyte with Ag/AgCl and a Pt foil as reference electrode and counter electrode, respectively. Cyclic voltammetry (CV) and galvanostatic charge/discharge (GCD) measurements were performed in a potential window of 0 to 1 V, and electrochemical impedance spectroscopy (EIS) was conducted in a frequency range of 10⁻⁵–100 kHz. The specific capacitance C (F g⁻¹) was calculated based on the GCD curves according to equation[1]:

$$C = \frac{I \times \Delta t}{m \times V} \quad (S1)$$

where I (A) and Δt (s) are the discharge current and time, respectively, m (g) represents of the active material's loading mass and V refers to the charge/discharge potential window.

6. Sodium diffusion coefficient calculation

The diffusion coefficient of Na⁺(D_{Na^+}) can be obtained from the low frequency line according to the formula :

$$D_{Na^+} = 0.5(RT/AF^2C\sigma)^2 \quad (S2)$$

where R , T , F , A , and C are the gas constant, the absolute temperature, the Faraday's constant, the apparent area of the electrode, and the molar concentration of Li⁺, respectively. σ is the Warburg factor following Equation[2] :

$$Z' = Re + Rct + \sigma\omega^{-\frac{1}{2}} \quad (S3)$$

where Re is the resistance between the electrolyte and electrode, and Rct is the charge transfer resistance. Thus, the slopes of the plot of Z' vs. $\omega^{-1/2}$ can used to obtain the values of σ .

7. Kinetic calculation

Capacitance contribution can be qualitatively analyzed according to CV curve, as shown below[3]:

$$i = av^b \text{ (S4)}$$

where i and v are the current density and the potential scan rate, respectively, a is a constant and b is a tunable parameter with a value of 0.5-1.0. When the value of b is close to 1.0, the reaction process is dominated by surface capacitance; when the value of b is close to 0.5, the reaction process is dominated by diffusion control. The b values of Ov-Mn₃O₄ electrode are 0.69 and 0.83, thus its charge storage dynamics are largely controlled by Faraday capacitance behavior (or insertion pseudocapacitance behavior).[4]

The contribution of capacitance and diffusion limit to the total capacitance is further quantified.

$$i(V) = k_1v + k_2v^{1/2} \text{ (S5)}$$

where k_1 and k_2 represent capacitive and diffusion contributions, respectively.

8. Supercapacitor devices measurements.

Supercapacitor Devices Measurements: Asymmetric supercapacitor (ASC) device was fabricated by employing Ov-Mn₃O₄ and AC as anode and cathode, respectively. Two electrodes were separated by glassy fibrous separator in 1 M Na₂SO₄ aqueous electrolyte. Cyclic voltammetry (CV) and galvanostatic charge/discharge (GCD) measurements were performed in a potential window of 0 to 2 V. Button supercapacitor was also fabricated by employing Ov-Mn₃O₄ and AC as anode and cathode. Small amount of electrolyte was added to complete the assembly of button supercapacitor.

The energy density (E , Wh kg⁻¹) of the ASC is calculated according to S6:[5]

$$E = \frac{C \times V^2}{2} \times \frac{1000}{3600} \text{ (S6)}$$

The power density (P , W kg⁻¹) of the ASC is calculated according to S7:

$$P = \frac{E \times 3600}{t} \quad (\text{S7})$$

where t (s) is discharge time.

9. Computational Details.

This calculation is based on the density function (DFT) method using the first quantum mechanical program VASP. The calculation uses a PBE functional based on the Generalized Gradient Approximation (GGA) exchange correlation approximation with the type of GGA PBE. In structural optimization, the plane wave cutoff energy is considered to be 500 eV. The convergence accuracy of the iterative process (SCF) is 10^{-5} . The strongest convergence exponent acting on an atom is 0.001 eV atom. When selecting K points for calculation, we choose 5X5X1 inverted space grid for calculation and the thickness of the vacuum layer is set to about 15 angstroms.

Figures

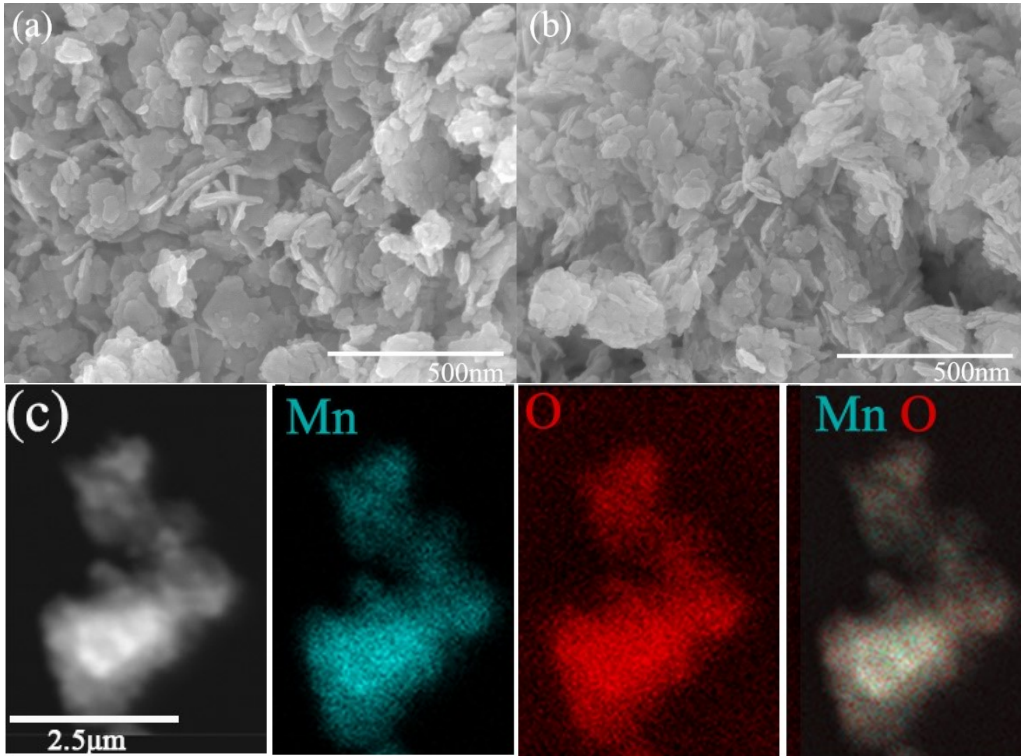


Figure S1. SEM images of the (a) Ov-Mn₃O₄ and (b) Mn₃O₄. (c) The elemental mapping images of Ov-Mn₃O₄.

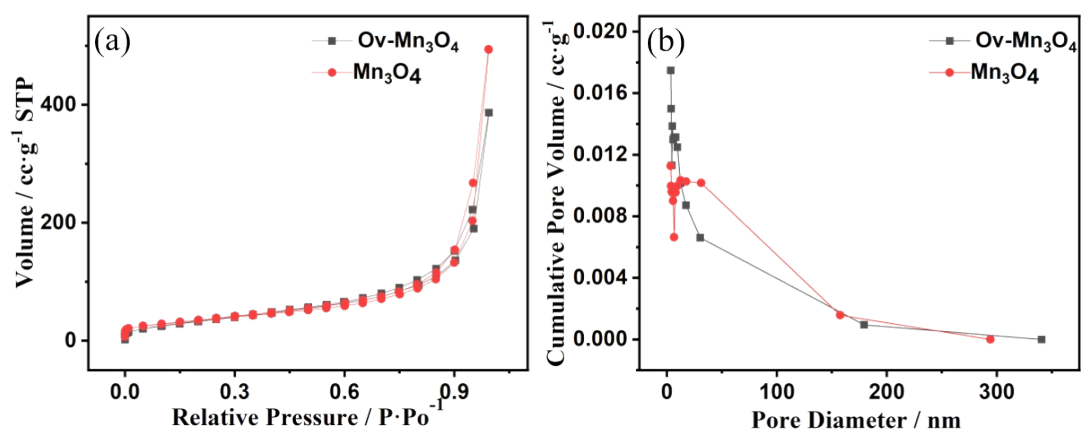


Figure S2. (a) Nitrogen adsorption–desorption isotherms and (b) pore size distributions of Ov-Mn₃O₄ and Mn₃O₄.

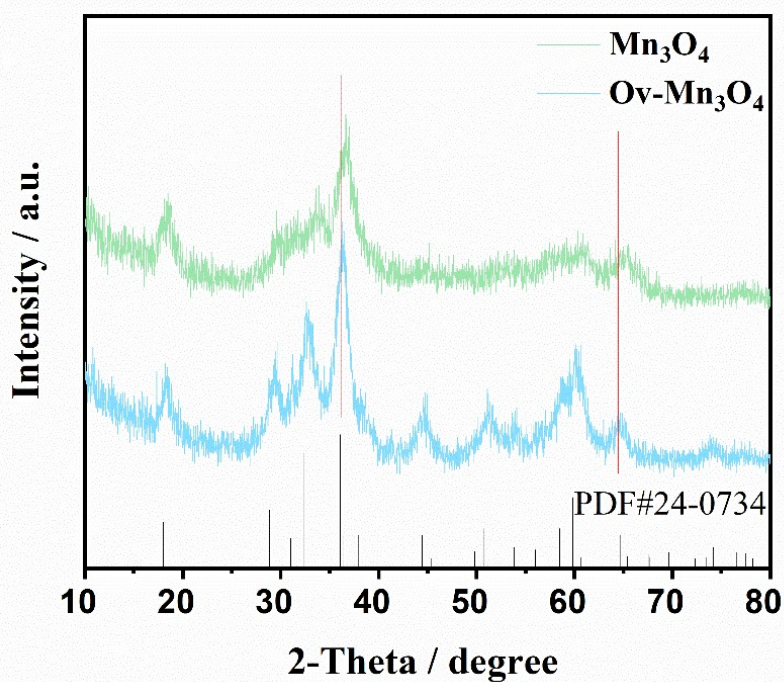


Figure S3. XRD images of Ov-Mn₃O₄ and Mn₃O₄

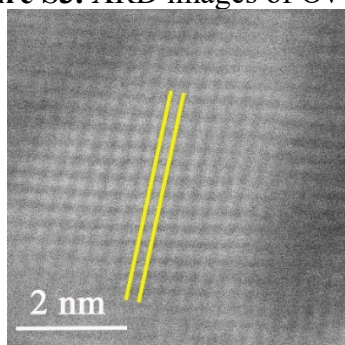


Figure S4. Spherical aberration electron microscopy images of Mn₃O₄.

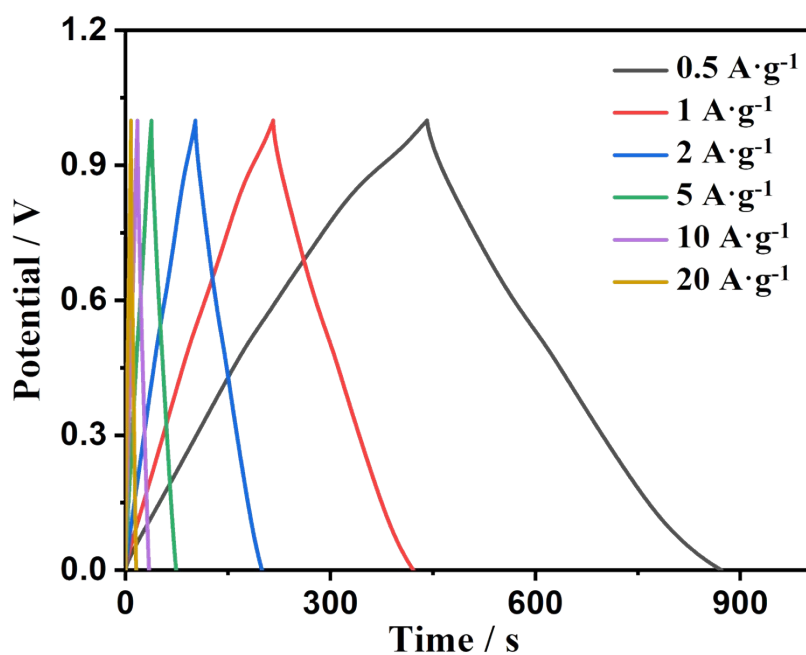


Figure S5. GCD curves of Mn₃O₄ under a current density from 0.5 A g⁻¹ to 10 A g⁻¹.

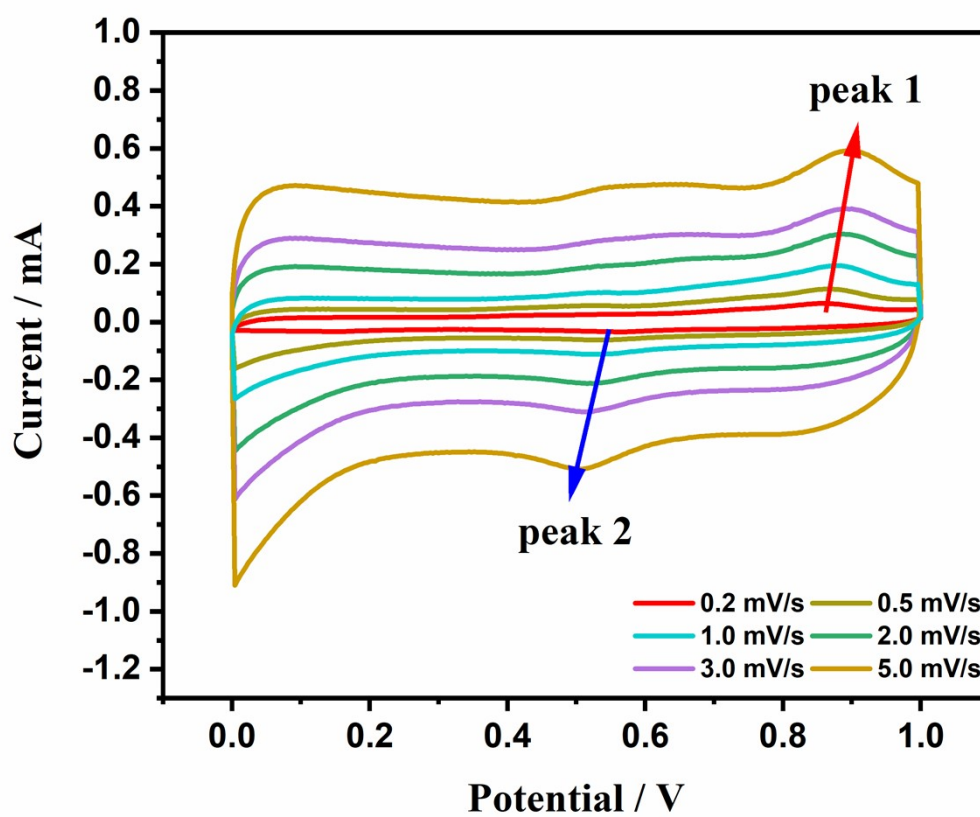


Figure S6. CV curves of ASC from 0.2 to 5 mV s⁻¹.

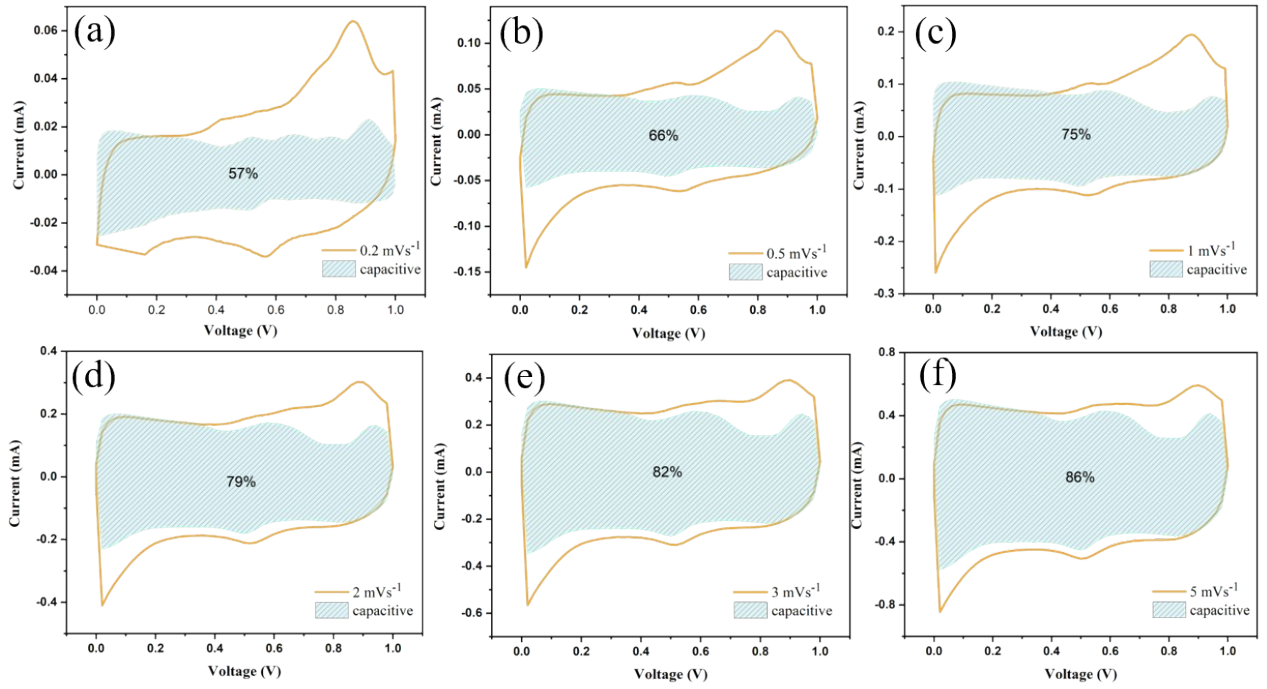


Figure S7. Capacitance contribution rate of Mn_3O_4 at different sweep speeds

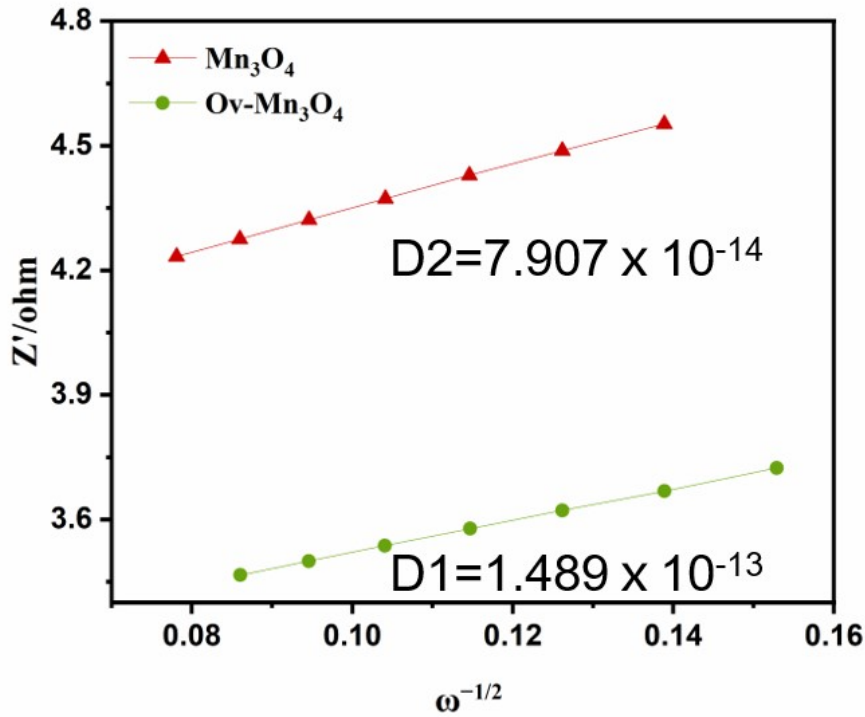


Figure S8. The plot of $\omega^{-1/2}$ versus $-\text{Im}(Z_w)$ according to EIS.

A randomly selected step from the GITT curve was considered to expound the mechanism. The Na^+ diffusion coefficient of all the samples is calculated as follows

$$D^{GITT} = \frac{4}{\pi\tau} \left(\frac{n_m V_M}{S} \right)^2 \left(\frac{\Delta E_S}{\Delta E_t} \right)^2$$

For compact electrode, S represents the electrode/electrolyte contact area; n_m is the mole number; V_m is the molar volume of the electrode material; t is the duration of the applied current pulse, and τ is the relaxation time. ΔE_s is the constant voltage change (V) caused by the current pulse. After removing the iR drop, ΔE_t is the potential change (V) in the steady-state current pulse. It is worth noting that Na^+ diffusion in the electrode is a visibly dynamic change process. The average Na^+ diffusivity values (D_{Na^+}) of Ov- Mn_3O_4 and Mn_3O_4 is about $3.1 \times 10^{-8} \text{ cm}^2\text{s}^{-1}$ and $1.1 \times 10^{-12} \text{ cm}^2\text{s}^{-1}$.

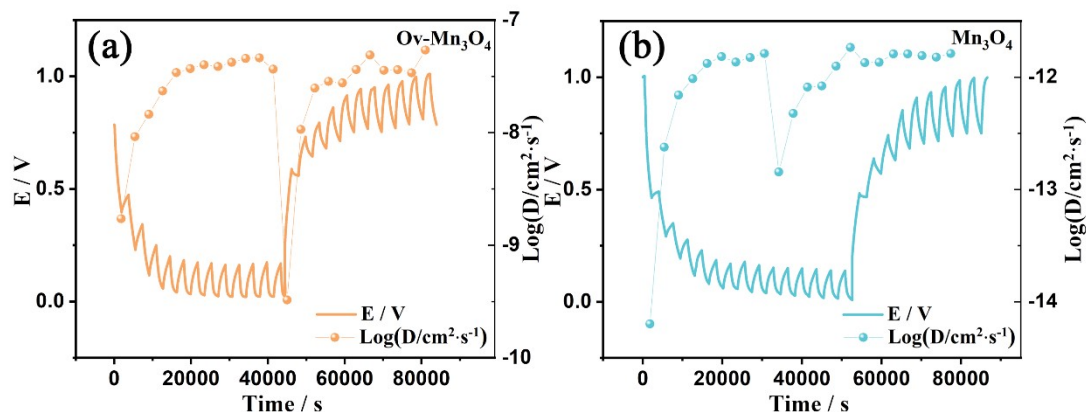


Figure S9. GITT voltage profile and the corresponding Na^+ diffusion coefficient of the (a) Ov- Mn_3O_4 and (b) Mn_3O_4 .

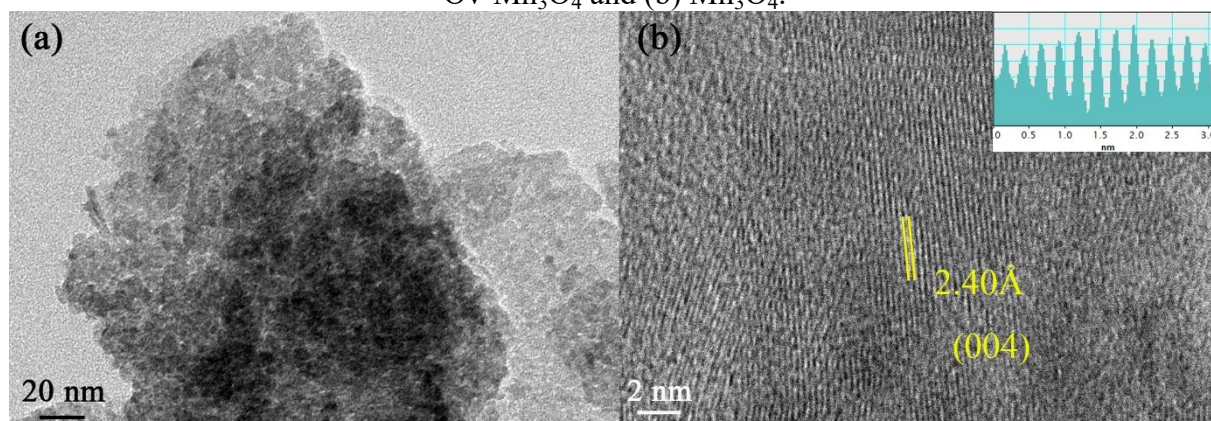


Figure S10. The TEM image (a) and HRTEM (b) image of the Ov- Mn_3O_4 after cycling.

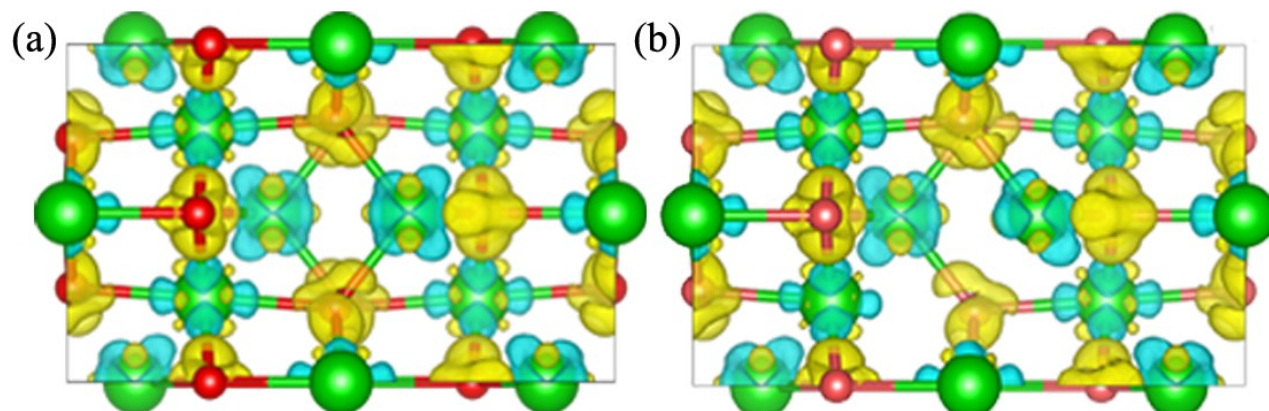


Figure S11. Charge density distribution of (a) Mn_3O_4 and differential charge density of (b) Ov- Mn_3O_4 .

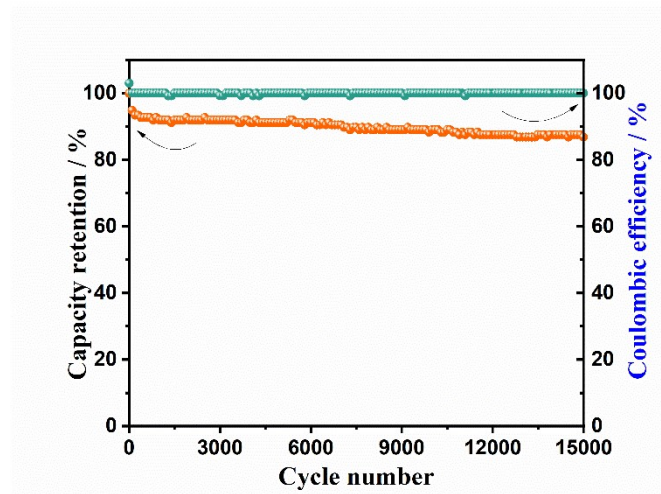


Figure S12 Coulomb efficiency and capacity retention curves of ASC.

Table S1. Refined crystallographic parameters by Rietveld analysis for Ov-Mn₃O₄ and Mn₃O₄.

	Space Group	a	b	c	α	β	γ	V Å ³	Rwp	Rp
Ov-Mn ₃ O ₄	I4 ₁ /amd	5.764	5.764	9.367	90.0	90.0	90.0	311.233	1.59 %	1.24%
Mn ₃ O ₄	I4 ₁ /amd	5.769	5.769	9.334	90.0	90.0	90.0	310.691	1.66 %	1.31%

Table S2 Fitting results of Mn₃O₄ and Ov-Mn₃O₄ samples obtained from the EIS curves

	Re(combined resistance)	Cdl(double-layer capacitance)	Rct(charge transfer resistance)	Zw(Warburg resistance)	CL(limit capacitance)
Ov-Mn ₃ O ₄	2.112	9.5×10 ⁻⁴	0.763	3.174	1.10×10 ⁻¹
Mn ₃ O ₄	2.144	2.8×10 ⁻³	2.249	3.567	1.53×10 ⁻¹

Table S3 Comparison of the Na⁺ storage capability between Ov-Mn₃O₄ and previously reported Mn-based cathode materials.

Mn-based materials	Specific capacitance (F/g)	Rate stability (%)	Cycle stability (%)	Electrolyte
Ov-Mn ₃ O ₄ (This work)	331.1 (1 A/g)	77.98 (1.0–20 A/g)	97 (2000 cycles)	1 M Na ₂ SO ₄
N-carbon Mn ₃ O ₄ [6]	122 (0.1 A/g)	43.38 (0.1–1.0 A/g)	94 (1000 cycles)	1 M Na ₂ SO ₄
Cr-doped Mn ₃ O ₄ [7]	272 (0.5 A/g)	22.78 (0.5–20 A/g)	70 (1000 cycles)	1 M Na ₂ SO ₄
Mn ₃ O ₄ @GR[8]	250 (1 A/g)	45.45 (0.5–10 A/g)	76 (1000 cycles)	1 M Na ₂ SO ₄
Porous Mn ₃ O ₄ [9]	229 (1 A/g)	81.72 (0.5–5 A/g)	78 (5000 cycles)	1 M Na ₂ SO ₄
RCDGO/Mn ₃ O ₄ [10]	187(1 A/g)	56.15 (0.05–2 A/g)	92 (1000 cycles)	1 M Na ₂ SO ₄

Table S4. Bader charge in Mn₃O₄, Ov-Mn₃O₄.

Models	Bader charge	
	Mn	O
Mn ₃ O ₄	-1.366	1.025
Ov-Mn ₃ O ₄	-1.284	1.027

Reference

- [1] L. Hu, R. Gao, A. Zhang, R. Yang, X. Zang, S. Wang, S. Yao, Z. Yang, H. Hao, Y.-M. Yan, Cu²⁺ intercalation activates bulk redox reactions of MnO₂ for enhancing capacitive performance, *Nano Energy*. 74 (2020). <https://doi.org/10.1016/j.nanoen.2020.104891>.
- [2] S. Wang, L. Li, Y. Shao, L. Zhang, Y. Li, Y. Wu, X. Hao, Transition-Metal Oxynitride: A Facile Strategy for Improving Electrochemical Capacitor Storage, *Adv Mater*. 31 (2019) e1806088. <https://doi.org/10.1002/adma.201806088>.
- [3] M. Han, J. Huang, S. Liang, L. Shan, X. Xie, Z. Yi, Y. Wang, S. Guo, J. Zhou, Oxygen Defects in beta-MnO₂ Enabling High-Performance Rechargeable Aqueous Zinc/Manganese Dioxide Battery, *iScience*. 23 (2020) 100797. <https://doi.org/10.1016/j.isci.2019.100797>.

- 
- [4] W. Guo, C. Yu, S. Li, X. Song, H. Huang, X. Han, Z. Wang, Z. Liu, J. Yu, X. Tan, J. Qiu, A Universal Converse Voltage Process for Triggering Transition Metal Hybrids In Situ Phase Restruction toward Ultrahigh-Rate Supercapacitors, *Adv Mater.* 31 (2019) e1901241. <https://doi.org/10.1002/adma.201901241>.
- [5] A. Zhang, R. Gao, L. Hu, X. Zang, R. Yang, S. Wang, S. Yao, Z. Yang, H. Hao, Y.-M. Yan, Rich bulk oxygen Vacancies-Engineered MnO_2 with enhanced charge transfer kinetics for supercapacitor, *Chem Eng J.* 417 (2021). <https://doi.org/10.1016/j.cej.2021.129186>.
- [6] Y. Gong, M.M. Zhang, W. Hua, J.L. Sun, H.F. Shi, P.G. Jiang, F.H. Liao, J.H. Lin, Metal-organic frameworks built from achiral 3-(5-(pyridin-4-yl)-4H-1,2,4-triazol-3-yl)benzoic acid: syntheses and structures of metal(II) complexes, *Dalton Trans.* 43 (2014) 145-151. <https://doi.org/10.1039/c3dt51736e>.
- [7] R. Dong, Q. Ye, L. Kuang, X. Lu, Y. Zhang, X. Zhang, G. Tan, Y. Wen, F. Wang, Enhanced supercapacitor performance of Mn_3O_4 nanocrystals by doping transition-metal ions, *ACS Appl Mater Interfaces.* 5 (2013) 9508-9516. <https://doi.org/10.1021/am402257y>.
- [8] M. Li, W. Xu, W. Wang, Y. Liu, B. Cui, X. Guo, Facile synthesis of specific FeMnO_3 hollow sphere/graphene composites and their superior electrochemical energy storage performances for supercapacitor, *J Power Sources.* 248 (2014) 465-473. <https://doi.org/10.1016/j.jpowsour.2013.09.075>.
- [9] F. Yang, M. Zhao, Q. Sun, Y. Qiao, A novel hydrothermal synthesis and characterisation of porous Mn_3O_4 for supercapacitors with high rate capability, *RSC Advances.* 5 (2015) 9843-9847. <https://doi.org/10.1039/c4ra10175h>.
- [10] F. Gao, J. Qu, Z. Zhao, Q. Zhou, B. Li, J. Qiu, A green strategy for the synthesis of graphene supported Mn_3O_4 nanocomposites from graphitized coal and their supercapacitor application, *Carbon.* 80 (2014) 640-650. <https://doi.org/10.1016/j.carbon.2014.09.008>.